Review of Scientific Instruments

High-resolution inelastic x-ray scattering at the high energy density scientific instrument at the European X-Ray Free-Electron Laser

Cite as: Rev. Sci. Instrum. **92**, 013101 (2021); https://doi.org/10.1063/5.0022886
Submitted: 24 July 2020 . Accepted: 12 December 2020 . Published Online: 04 January 2021

L. Wollenweber, T. R. Preston, A. Descamps, V. Cerantola, A. Comley, J. H. Eggert, L. B. Fletcher, G. Geloni, D. O. Gericke, S. H. Glenzer, S. Göde, J. Hastings, O. S. Humphries, A. Jenei, O. Karnbach, Z. Konopkova, R. Loetzsch, B. Marx-Glowna, E. E. McBride, D. McGonegle, G. Monaco, B. K. Ofori-Okai, C. A. J. Palmer, C. Plückthun, R. Redmer, C. Strohm, I. Thorpe, T. Tschentscher, I. Uschmann, J. S. Wark, T. G. White, K. Appel, G. Gregori, and U. Zastrau

AIP Publishing

Review of Scientific Instruments ARTICLE scitation.org/journal/rsi

High-resolution inelastic x-ray scattering at the high energy density scientific instrument at the European X-Ray Free-Electron Laser

Cite as: Rev. Sci. Instrum. 92, 013101 (2021); doi: 10.1063/5.0022886
Submitted: 24 July 2020 • Accepted: 12 December 2020 •
Published Online: 4 January 2021 • Publisher Error Corrected: 7 January 2021

L. Wollenweber,[1,a] T. R. Preston,[1] A. Descamps,[2,3] V. Cerantola,[1] A. Comley,[4] J. H. Eggert,[5] L. B. Fletcher,[2] G. Geloni,[1] D. O. Gericke,[6] S. H. Glenzer,[2] S. Göde,[1] J. Hastings,[2] O. S. Humphries,[7] A. Jenei,[5] O. Karnbach,[7] Z. Konopkova,[1] R. Loetzsch,[8] B. Marx-Glowna,[8] E. E. McBride,[2] D. McGonegle,[7] G. Monaco,[9] B. K. Ofori-Okai,[2] C. A. J. Palmer,[10] C. Plückthun,[1] R. Redmer,[11] C. Strohm,[1,12] I. Thorpe,[1] T. Tschentscher,[1] I. Uschmann,[8,13] J. S. Wark,[7] T. G. White,[14] K. Appel,[1] G. Gregori,[7] and U. Zastrau[1]

AFFILIATIONS

[1]European XFEL, Holzkoppel 4, 22869 Schenefeld, Germany
[2]SLAC National Accelerator Laboratory, 2575 Sand Hill Road, Menlo Park, California 94025, USA
[3]Department of Aeronautics and Astronautics, Stanford University, Stanford, California 94305, USA
[4]Atomic Weapons Establishment, Aldermaston, Reading, Berkshire RG7 4PR, United Kingdom
[5]Lawrence Livermore National Laboratory, 7000 East Avenue, Livermore, California 94550, USA
[6]Centre for Fusion, Space & Astrophysics, Department of Physics, University of Warwick, Coventry CV4 7AL, United Kingdom
[7]Department of Physics, Clarendon Laboratory, University of Oxford, Parks Road, Oxford OX1 3PU, United Kingdom
[8]Institut für Optik und Quantenelektronik, Friedrich-Schiller-Universität Jena, Max-Wien-Platz 1, 07743 Jena, Germany
[9]Dipartimento di Fisica, Universita di Trento, via Sommarive 14, Povo 38123, TN, Italy
[10]School of Mathematics and Physics, Queen's University Belfast, University Road, BT7 1NN Belfast, United Kingdom
[11]Universität Rostock, Institut für Physik, Albert-Einstein-Straße 23-24, 18051 Rostock, Germany
[12]Deutsches Elektronen-Synchrotron DESY, Notkestraße 85, 22607 Hamburg, Germany
[13]Helmholtz-Institut Jena, Fröbelstieg 3, 07743 Jena, Germany
[14]Physics Department, University of Nevada at Reno, Reno, Nevada 89506, USA

[a]**Author to whom correspondence should be addressed:** lennart.wollenweber@xfel.eu

ABSTRACT

We introduce a setup to measure high-resolution inelastic x-ray scattering at the High Energy Density scientific instrument at the European X-Ray Free-Electron Laser (XFEL). The setup uses the Si (533) reflection in a channel-cut monochromator and three spherical diced analyzer crystals in near-backscattering geometry to reach a high spectral resolution. An energy resolution of 44 meV is demonstrated for the experimental setup, close to the theoretically achievable minimum resolution. The analyzer crystals and detector are mounted on a curved-rail system, allowing quick and reliable changes in scattering angle without breaking vacuum. The entire setup is designed for operation at 10 Hz, the same repetition rate as the high-power lasers available at the instrument and the fundamental repetition rate of the European XFEL. Among other measurements, it is envisioned that this setup will allow studies of the dynamics of highly transient laser generated states of matter.

I. INTRODUCTION

Inelastic X-ray Scattering (IXS) is a powerful tool to measure material dynamics by comparing the energy and momentum of a photon before and after the interaction process. The accessible processes can be categorized by the value of the energy transfer and range from keV individual electron responses in Compton scattering processes[1–3] through collective electronic excitations such as plasmons and x-ray Raman scattering in the eV range[4–6] down to structural dynamics on the order of meV.[7–10] Consequently, IXS has become a well-established technique at many facilities in the past few decades.[11–13] Developments in high-resolution IXS at synchrotron radiation sources, in conjunction with neutron scattering techniques,[14] have enabled the elucidation of many processes in the field of condensed matter physics. Energy transfers in the range of a few meV give access to detailed measurements of phonons in crystalline[15] materials and collective dynamics in non-crystalline materials.[15] The technique can also be applied to studies of phase transitions in conditions relevant to the interior of the Earth[16,17] and the effect of magnetism on lattice dynamics.[18]

With the emergence of X-Ray Free-Electron Lasers (XFELs) as a new intense radiation source with femtosecond pulse-lengths, many established techniques have successfully been transferred from synchrotron radiation sources to XFELs. The combination of XFELs and synchronized optical lasers enables pump–probe measurements of previously inaccessible processes in short-lived and extreme states of matter generated by optical lasers.[19–22] In particular, for energy transfers in the eV range, measurements of plasmon excitations in shock compressed matter on a ns timescale[23,24] and the dielectric function of isochorically heated matter[25] have been successfully demonstrated. Recently, high-resolution IXS has been realized at the Linac Coherent Light Source (LCLS) with tens of meV resolution, allowing measurements of phonon-modes in polycrystalline diamond.[26]

Simultaneous measurement of the energy and momentum transfer in materials gives access to the dynamical structure factor $S(\vec{k}, \omega)$, where $\vec{k} = \vec{k}_{out} - \vec{k}_{in}$ is the momentum transfer and ω is the frequency change due to the scattering process. This contains a wealth of information on the fundamental properties of the dynamic states probed, such as atomic and ionic motion,[27] sound velocity,[28] dissipative macroscopic phenomena such as viscosity, and thermal conductivity.[29] Moreover, this technique at high resolution can resolve small energy and momentum transfers and thus enables direct temperature measurements of temperatures below 1 eV either through Doppler broadening or by measurements of Stokes/anti-Stokes lines in detailed balance.[30] Additionally, by comparing these to the intensity of the elastic scattering, it is possible to determine diffusive modes in amorphous materials and plasmas.[31] To facilitate these future measurements, a high-resolution IXS setup has been incorporated into the High Energy Density (HED) scientific instrument at the European XFEL[32,33] with a measured resolution of ~45 meV, which should allow typical IXS features in matter at extreme conditions to be resolved while having a sufficient transmission for the required photon statistics.

II. SETUP

The setup is conceptually based on the successful design used at the LCLS, as described by McBride *et al.*[26] It is located at the HED instrument at the hard x-ray SASE 2 undulator of the European XFEL.[34,35] The accelerator driving the light source accelerates electron macro-bunches at a base rate of 10 Hz. Each of the macro-bunches can contain between 1 and 2700 electron bunches separated by a minimum time of 220 ns. This enables x-ray pulses at a maximum repetition rate of 4.5 MHz within such a bunch train. For the experiment described here, the x-ray source was operated in a single bunch self-amplified spontaneous emission (SASE) mode at a repetition rate of 10 Hz with a photon energy centered at 7.49 keV and a bandwidth of roughly 20 eV. The average pulse energy was 1 mJ after the source, measured by a gas monitor.[36]

To reduce the incident bandwidth of the SASE beam, the x rays were sent through two stages of monochromatization (Fig. 1), which all use symmetrical Bragg reflections. The first stage comprises a two-bounce quasi channel-cut Si (111) monochromator.[37] This monochromator can be cryogenically cooled to 70 K to reduce the effects of thermal expansion under irradiation by the intense x rays and serves primarily as a pre-monochromator for the following monochromator. For this experiment, it was operated at room temperature. The second monochromator employs a Si (533) channel-cut crystal, which was manufactured by the x-ray optics group of the Friedrich-Schiller University Jena. Its channel width of 106 mm is adapted to the Si (111) pre-monochromator to roughly compensate the vertical offset imposed by the first monochromator at a photon energy of 7.49 keV at the corresponding Bragg angle of 87.9°. Ensuring a zero offset to the nominal beamline has the advantage that the following beamline and diagnostics, as well as laser optics in the experimental chamber, require no re-alignment when using the monochromatized beam. Under these conditions, the energy width of the incident beam would be reduced to a value of 30.8 meV or a bandwidth $\Delta E/E$ of 4×10^{-6}. Offline measurements with a double crystal diffractometer showed a broadening smaller than 10% of the theoretical rocking curve width. The Si (533) reflection was chosen because it yields the necessary resolution while having no lower order reflections. This is particularly important when using the setup to study warm-dense matter states, as the plasma emission could add strongly to the noise on the IXS signal. For example, when using the Si (444) reflection at a XFEL photon energy of 7.912 keV, the scattering setup will also transmit via the Si (111) reflection at a quarter of the photon energy, 1.978 keV, which is emitted from the ablation plasma.

The Si (533) channel-cut crystal was cut from a monolithic ingot. The surfaces were sawn with a diamond blade and subsequently polished with SiC of decreasing grain size. Afterward, the crystal was etched in a mixture of hydrofluoric acid, acetic acid, and nitric acid for 20 min. To increase the flatness of the surfaces, the crystal was polished a second time with 38 μm SiC, followed by the same etching process.

Despite this, optical wavefront measurements yield a surface roughness with a root-mean-square (rms) value of ~5 μm and a peak-to-valley (PV) value of ~20 μm. In comparison, the Si (111) crystals of the first monochromator stage were highly polished, which is technically possible because the crystals are separated in a quasi channel-cut, and have a rms roughness of order 30 nm with a PV value on the order of 200 nm. Nevertheless, the two reflections from the Si (533) crystal preserve the spatial profile of the beam (Fig. 2),[38] most likely due to the high Bragg angle of ~88°.

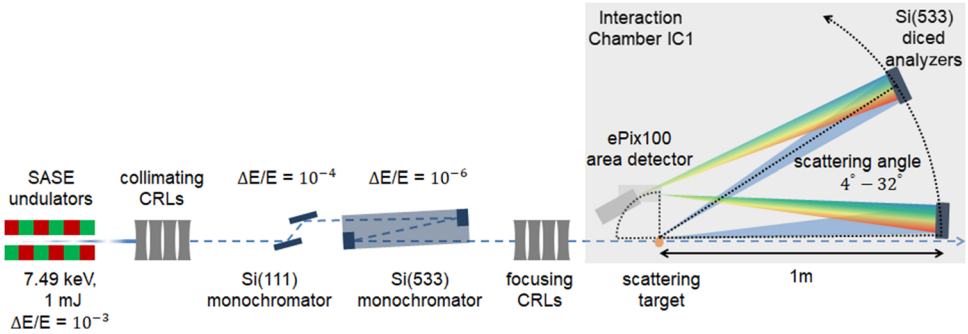

FIG. 1. The key elements of the setup in a side view. The x-ray beam originating from the undulators to the left is sent through a set of CRLs to collimate the beam. Then, the beam is sent through a two-bounce Si (111) monochromator, reducing its energy width from the 20 eV SASE width to ~0.7 eV. Afterward, the beam passes a Si (533) monochromator to reduce its bandwidth to 30.5 meV. This monochromatized beam can be focused down to a range of different sizes at the sample location through the combination of various CRL sets. In the target chamber, the scattered x rays from the target are collected and focused by three spherically bent diced analyzer crystals. An ePix100 detector is mounted above the target to record the signal. Together, these three elements form a Rowland circle of 1 m diameter. Both the analyzers and detector are mounted onto curved rails to enable a variation of the scattering angle θ between 4° and 32°.

One of the main goals of the high-resolution IXS setup is to study extreme states of matter generated by optical drive lasers. The Helmholtz International Beamline for Extreme Fields at the European XFEL (HIBEF) user consortium has contributed two high-power lasers to the HED scientific instrument,[39,40] which runs at a maximum repetition rate of 10 Hz. Because of this, the monochromator was designed to match this repetition rate. Higher pulse rates would be a rare case for these experiments, as, even at 4.5 MHz, the extreme state will have disappeared before the next pulse arrives after 220 ns. At 10 Hz, the time between two pulses is sufficient to dissipate the heat deposited by the x-ray pulse at the location of the first reflection into the crystal bulk and support structures. Therefore, there is no loss of intensity between pulses due to the expansion of the lattice spacing at the first reflection, and the Darwin curves overlap at 10 Hz. In this early stage of instrument operation, we were not able to study the transmission at repetition rates above 10 Hz, as the cryogenic cooling of the Si (111) monochromator was not yet operational, without which the transmission of a pulse train is significantly reduced.

Both monochromators are located roughly 120 m upstream of the experimental chamber and 850 m downstream of the undulator exit. A set of beryllium compound refractive lenses (CRLs)[41] is located 230 m after the undulator, which was used to collimate the x-ray beam. Repeated measurements of the beam's spatial profile at different locations along the beam propagation have yielded a vertical divergence, which is the dispersive direction of the monochromators, of ≤1 μrad for this collimated beam. Thus, a further reduction of the divergence by asymmetric reflections, often necessary on high-resolution monochromators at synchrotron radiation sources, where the divergence can be of the order of the crystal rocking curve, is not required for this setup. Final focusing can be achieved by using one of the two CRL sets installed downstream of the monochromators. For this experiment, we used a CRL set located 9 m upstream of the interaction point. It was used to focus the beam down to a spot size of ~25 μm at the target in the interaction chamber IC1 in the experimental hutch. Smaller spot sizes below 10 μm are possible with this lens set. Another set of CRLs, which were not used in this experiment, is located directly after the

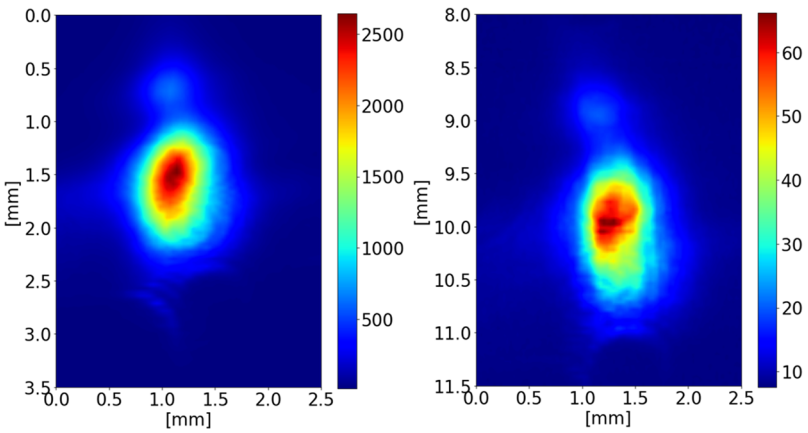

FIG. 2. A comparison of the beam profiles 80 m after the monochromators on a YAG-screen. On the left side is displayed the beam after two reflections from the highly polished Si (111) crystals. The right side shows the beam after the additional Si (533) monochromator without high quality polishing. Both images show the average over roughly 1800 shots of the FEL. This demonstrates that the spatial profile of the coherent FEL beam is preserved by the Si (533) channel-cut monochromator.

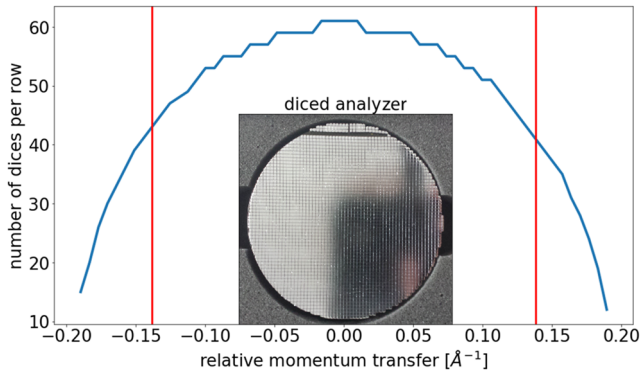

FIG. 3. Due to the size of the analyzer crystals, the detector signal is an integration over a range of different k-values, where each row of dices contributes to a different momentum transfer compared to the central row. The blue line shows how many dices contribute to a specific relative momentum transfer to the central row of the central analyzer. The two red vertical lines indicate the central 75% area we assume in our analysis. The inset shows a photograph of one of the diced analyzer crystals.

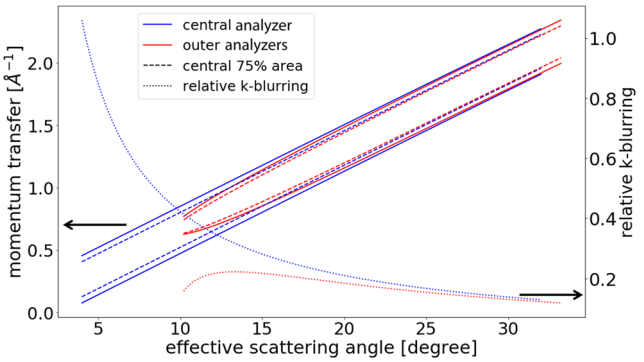

FIG. 4. The signal on the detector is the result of an integration over a range of momentum transfers due to the size of the analyzer crystals. The solid and dashed lines show the accepted k-range (left axis) for the middle (blue) and outer (red) analyzers for their effective scattering angle. For the middle analyzer, this is the angle of the curved rail. The solid lines show the accepted range over the complete analyzer diameter, while the dashed lines show the accepted range of the inner 75% of the analyzers. Because of the off-axis angle, the outer analyzers have a higher minimum momentum transfer. At the same time, they have a lower relative blurring compared to the analyzer center, as indicated by the dotted lines (right axis). This enables, for a certain range of momentum transfers, two ways of measurements. First, at a higher angle of the curved rails with the middle analyzers. The second is at a lower angle with the two outer analyzers with lower relative k-blurring but also lower individual intensity due to the angular dependence of the scattering cross section in the case of the horizontally polarized x rays.

monochromators and can focus to a few tens of micrometers at the sample location.

In this chamber, three spherical diced analyzer crystals[42–44] (Fig. 3, inset) using the same Si (533) reflection as the monochromator were mounted to a vertical curved-rail system with a radius of 1 m (Fig. 1) in a Rowland-circle geometry.[45–48] One was sitting centered over the primary x-ray beam path (blue dotted line, Fig. 1), and two others were sitting at the same height but offset to the left and right at an angle of $\phi = 9.4^\circ$ to the primary beam axis. The usage of three analyzers shortens the measurement time and decreases the necessary number of samples in the case of destructive experiments, e.g., dynamic compression. Due to the off-center positions of the two analyzers, the setup measures two momentum transfer values simultaneously, which can be matched to a phonon dispersion curve as demonstrated by Descamps *et al.*[30] With the curved rail, it is possible to change the scattering angle between 4° and 32° without breaking vacuum. These angles correspond to scattering wavenumbers $k = |\vec{k}|$ from 0.26 Å^{-1} to 2.01 Å^{-1} at the incident photon energy of 7.49 keV. This way, it is possible to conduct measurements at different momentum transfers while keeping all other conditions constant with minimal realignment. A suitable use case is, for example, the measurement of the dispersion $\omega(k)$ of collective excitations to study the effects of local field corrections.[24] The analyzer crystals have a diameter of 100 mm, a bending radius of 1 m, and a dice size of 1.65 × 1.65 mm^2, giving a calculated spectral window of 460 meV. The foci of the analyzers in the SASE beam show the square shapes [Fig. 5(a)] expected when the Rowland-circle geometry is fulfilled. However, all three squares have a width slightly smaller than the expected 3.3 mm = 2 × 1.65 mm^2, from left to right 3.1 mm, 3.2 mm, and 3.2 mm. A possible reason for this is a small mismatch of the Rowland-circle, which results in a demagnification of the detector image and decreased reflectivity at the edges of the sawn dices.

Due to the large size of the analyzers, the collected signal results from an integration over a range of different k-values. In the lowest angular position, this leads to a blurring of 0.26 ± 0.19 Å^{-1} for the middle analyzer and $0.68^{+0.09}_{-0.05}$ Å^{-1} for the outside analyzers (Fig. 4). As two of the analyzers are not in line with the incident beam axis, their effective scattering angle $\theta_{eff} = \arccos(\cos(\theta) \cdot \cos(\phi))$ is a combination of the curved rail angle θ and the fixed angle $\phi = 9.4^\circ$ resulting from the mounting. Thus, the two outer analyzers have a higher minimum scattering vector than the central analyzer. Additionally, their relative k-blurring is smaller than that of the central analyzer at the cost of a lower intensity of the scattered radiation on the analyzers due to the angular dependence of the scattering cross section for horizontally polarized x rays, shown by the dotted lines (Fig. 4). Due to the spherical aperture of the crystals, there are fewer dices along the outer edges of the crystals that scatter photons at larger differences to the central k-value. Additionally, we masked the outer edge of the analyzers with aluminum foil to cover up possible damaged diced sections at the edges. Therefore, we assume that most photons contributing to the signal are reflected from the central 75% of the area (Fig. 3). Then, the blurring would be on the order of ±0.16 Å^{-1} in the middle and $^{+0.08}_{-0.05}$ Å^{-1} on the left and right analyzers, as indicated by the dashed lines (Fig. 4).

Finally, the scattered radiation was recorded on an ePix100[49] detector with 768 × 704 pixel^2 and a pixel size of 50 μm. The detector was mounted on the innermost curved rail, 80 mm above the sample, and running at a repetition rate of 10 Hz. In this geometry, the sample, analyzers, and the detector form a Rowland circle of R = 1 m diameter. Since the center of rotation of each rail is aligned to the interaction point of x rays and the scattering target, it is possible to keep this geometry while changing the scattering angle with the curved rail system. Alternatively, the analyzers can be mounted to a rail upstream of the sample, allowing measurements at higher

momentum transfers. The complete setup is kept at a typical vacuum level of 10^{-4} mbar to enable compatibility with high-intensity and high-power laser experiments.

III. DISPERSION AND ENERGY RESOLUTION

Working at large Bragg angles in near-backscattering geometry $\Theta \sim 90^\circ$ ensures a high dispersion and resolution. The exact value of the Bragg angle is strongly dependent on the photon energy near 90°, as given by Bragg's law $\lambda = 2d \sin(\Theta)$. Here, λ is the x-ray wavelength and $2d$ is twice the inter-planar distance of the reflection: 1.656 446 Å[50] in the case of Si(533). Subtle differences in the x-ray wavelength $\Delta\lambda$ relate to significant changes in Bragg angle $\Delta\Theta$ and thus positions on an area detector via the differential Bragg equation,

$$\frac{\Delta\lambda}{2\,d\cos(\Theta)} = \Delta\Theta, \tag{1}$$

as near 90°, $\cos(\Theta)$ is small. Furthermore, the relative spectral resolution

$$\frac{\Delta\lambda}{\lambda} = \frac{\Delta\theta}{\tan(\Theta)}, \tag{2}$$

where $\Delta\theta$ is the Darwin width of the reflection and is smallest at large Bragg angles. Even though the Darwin width gets wider near 90°, this is compensated by the $1/\tan\Theta$ term approaching zero. To interpret spectral measurements, it is therefore crucial to know the absolute photon energy.

We determined the photon energy by comparing the positions of the beam after the Si (111) monochromator and the beam after both the Si (111) and Si (533) monochromators on a screen located 80 m downstream. After averaging over a few thousand shots, the Bragg angle of 87.85° ± 0.05° can be calculated geometrically from the offset and the known length of the channel-cut of 106 mm. From the Bragg angle, the photon energy was determined to be 7490.2 ± 0.2 eV.

To determine the energy dispersion of the monochromator, the same procedure was repeated for slightly different Bragg angles in a range of ±0.02°. Afterward, we scanned the same Bragg angles with a scattering target in the experimental chamber. With the differences in incident photon energy, this leads to a change of position of the radiation dispersed by the analyzer on the detector [Figs. 5(b)–5(d)]. The combination of the two measurements yields a dispersion value of 7.7 ± 0.5 meV/pixel on the detector, which is equivalent to 0.15 meV/μm. The largest contributions to the error for this measurement are the beam jitter and motor backlash of the axis, which changes the Bragg angle. On the contrary, the photon energy can be calculated from the dispersion as the dispersion is determined by photon energy E, Bragg angle Θ, and Rowland circle diameter R,

$$\frac{\Delta E}{\Delta x} = \frac{E}{2\,R\,\tan(\Theta)}. \tag{3}$$

This way, the dispersion value of 0.15 meV/μm yields a photon energy of 7490.95 eV. To match the previously obtained photon energy of 7490.2 eV, the dispersion should have a value of 0.141 meV/μm. This value still lies at the edge of the 6% error of

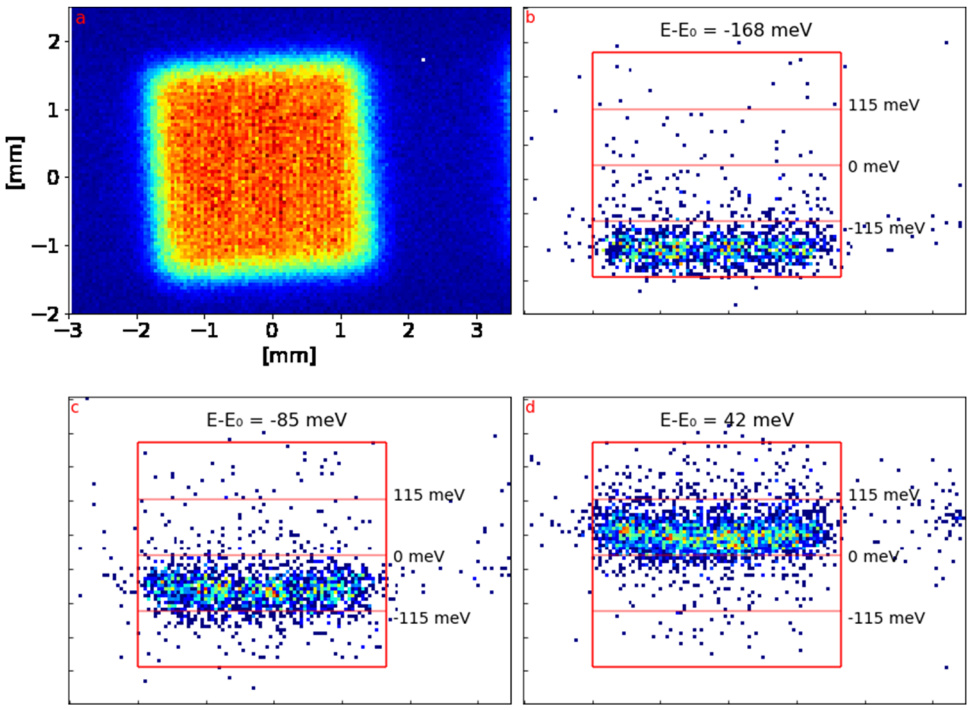

FIG. 5. The observed focus of the central analyzer using the SASE beam (a) and for different Bragg angles of the Si (533) monochromator, where the position changes with the incident photon energy [(b)–(d)]. A more complete series of these images was used to determine the energy dispersion of the setup.

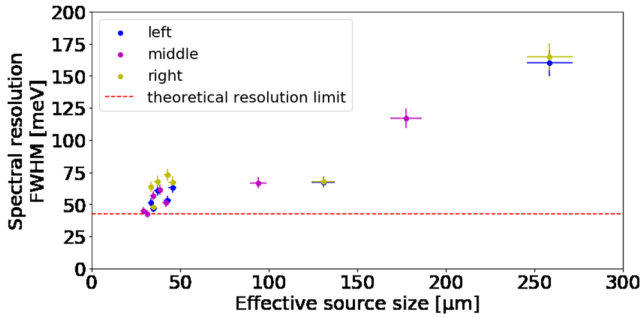

FIG. 6. Overview of the quasielastic scattering data. The resolution is given as the FWHM value of a pseudo-Voigt function fitted to the data. The effective source size describes the combination of sample illumination, thickness, and viewing angle. Clearly, the thicker targets show a worse resolution due to source broadening. In addition, the two outer analyzer crystals (blue and yellow) have a lower resolution than the middle analyzer (purple) because of the larger effective source size at higher scattering angles. The red dotted line indicates the fundamental lower limit for the resolution: the convolution of monochromator and analyzer Darwin curves. This was almost achieved with a 50 μm thick PMMA sample. Thus, thinner targets should not suffer from source broadening, and the resolution will be only limited by the setup.

our measured value. In addition, a mismatch of the Rowland circle and inaccuracies in the analyzers' bending radii, which we did not measure accurately, both add an uncertainty to Eq. (3).

Using various samples and changes of the scattering angle, we collected the quasielastic scattering signal from different thicknesses (50 μm, 500 μm, and 1100 μm) of polymethylmethacrylate (PMMA, Goodfellows Ltd.) and fused silica to characterize the instrument resolution for each set of conditions (Fig. 6). The effective source size is given by $t \cdot \sin(\theta_{eff}) + a \cdot \cos(\theta_{eff})$, where t is the sample thickness and a is the focus size on the sample, with θ_{eff} as defined earlier for the outer analyzers and equal to θ for the central analyzer. For quantification, we take the full width at half maximum (FWHM) of the quasielastic peak as the instrument function, as PMMA has

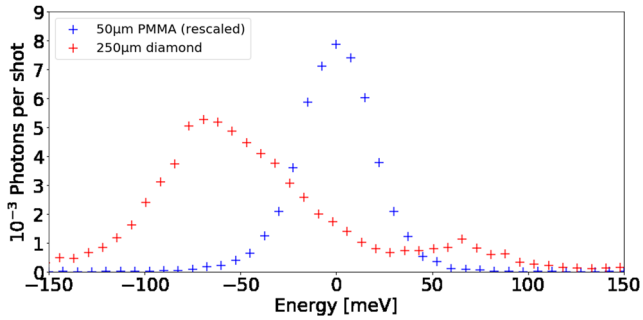

FIG. 7. Measured spectra from 50 μm PMMA (blue) and 250 μm single crystal diamond (red). The elastic signal from the PMMA shown here is reduced by a factor of 10. As it is a perfect single crystal, there is no quasielastic scattering from the diamond. Instead, there are the peaks corresponding to phonon creation and annihilation. The diamond spectrum is reproduced with permission from Descamps *et al.*, "An approach for the measurement of the bulk temperature of single crystal diamond using an x-ray free electron laser," Sci. Rep. **10**, 14564 (2020). Copyright 2020 Springer Nature Limited.

TABLE I. Contributions to the overall resolution. It is assumed that all entries possess a Gaussian shape. The Si (533) Darwin width in the monochromator and analyzers is the biggest contributor.

Contribution	ΔE (meV)
Incident bandwidth	30
Analyzer	30
Pixel size	7
Source size	7
Total	44

only low-energy and strongly damped modes, which our setup cannot resolve. Generally, the spectra from the outer analyzers show a slightly worse resolution than the central analyzer because the projected source size is larger for the outer analyzers. This leads to a reduced resolution due to source broadening, where the analyzers collect radiation from different source points. A similar effect can be observed when thicker samples are used.

We achieved the highest resolution of 44 ± 3 meV by using a 50 μm PMMA sample [Fig. 7 (blue)] with a photon count of 3.8 photons per shot. Here, the largest contribution to the error comes from the uncertainty on the dispersion. This value is very close to the convolution of the incident bandwidth and Darwin width of the analyzers at 42.8 meV, which are the two largest contributors to the overall resolution, as can be seen from Table I. If other factors such as pixel and source size are included, the measured 44 meV is precisely the expected resolution under the assumption that these factors contribute with a Gaussian shape. We could only estimate the size and shape of the incident x-ray focus spot with 10 μm precision. Consequently, there remains some uncertainty on the source size contribution. Using the same setup, we measured inelastic scattering from phonons in single crystal diamond [Fig. 7 (red)], where an average of 0.5 photons per shot was achieved. These data were published by Descamps *et al.*[30] to demonstrate the capability of the setup to perform accurate temperature measurements via detailed balance.

IV. PULSE LENGTH CONSIDERATIONS

Ultra-short electromagnetic pulses, such as the ones from a XFEL, require a sufficiently broad frequency spectrum. Thus, strong monochromatization may lead to an increase in the pulse duration. We know that the pulses after the monochromators have a bandwidth of 30.5 meV. If we assume a Gaussian profile, a Fourier-transform-limited pulse of 1 fs duration has a bandwidth of 1.83 eV. Therefore, a non-chirped FEL pulse with a Gaussian distribution monochromatized with a bandwidth of 30.5 meV FWHM would correspond to a duration of about 60 fs. Any chirp present in the monochromatized pulse would increase its duration for a fixed bandwidth, but such an effect is estimated to be small. In comparison, we can take the length of the electron bunches, which was measured to be slightly shorter than 50 fs,[33] as a maximum duration for any SASE pulse. We thus conclude that, during our experiment, the FEL pulse duration was determined by the bandwidth of the monochromator and that the pulses are somewhat lengthened due to monochromatization. However, after monochromatization, the

pulses are closer to transform-limited and possess an increased temporal coherence. The slightly longer pulses do not pose a limitation for any planned experiment on structural properties.

V. CONCLUSION

We have successfully demonstrated a new capability of the HED instrument to resolve inelastic x-ray scattering with a spectral resolution of 44 meV. This resolution was achieved through a two-stage monochromatization of the SASE beam at 7.49 keV: first by a Si (111) quasi channel-cut, followed by a Si (533) channel-cut monochromator. The scattered radiation was collected by three Si (533) diced analyzer crystals and focused on a position resolving detector. This setup can be used to measure collective features such as acoustic phonon modes, for example, in diamond and determine its temperature by detailed balance, as demonstrated by Descamps *et al.*[30] The target chamber also offers the possibility to mount an analyzer in backscattering geometry, allowing the measurement of meV-broadening due to scattering from individual electrons in the non-collective regime. In the near future, self-seeding[51] will be available at the SASE2 undulator. As the following calculation demonstrates, this will lead to a higher number of photons after monochromatization. The Si (111) monochromator will be able to transmit almost the complete incident spectrum with several 100 μJ pulse energy and ~1 eV seeded bandwidth. This will result in a pulse energy of order 10 μJ or 8.3×10^9 photons per pulse in 35 meV bandwidth after the Si (533) monochromator in comparison to the average of 1 μJ from the SASE pulses. This capability together with the short pulse-lengths of XFELs will enable the production of snapshots from materials under extreme conditions and will be uniquely suited to constraining equation-of-state (EOS) measurements on highly transient plasmas generated with the HIBEF high-intensity and high-energy lasers at the HED instrument at the European XFEL.

ACKNOWLEDGMENTS

We acknowledge the European XFEL in Schenefeld, Germany, for provision of x-ray free-electron laser beamtime at the Scientific Instrument HED (High Energy Density Science) and would like to thank the staff for their assistance. The authors are indebted to the HIBEF user consortium for the provision of instrumentation and staff that enabled this experiment. K.A., T.T., and R.R. acknowledge support from the DFG (Grant No. FOR 2440). Z.K. and C.P. acknowledge support from the DFG Project KO-5262/1. A.D. acknowledges funding from the National Science Foundation under Grant No. 163270. We further acknowledge that this work was supported by the Department of Energy, Laboratory Directed Research and Development program at the SLAC National Accelerator Laboratory under Contract No. DE-AC02-76SF00515 and as part of the Panofsky Fellowship awarded to E.E.M. Furthermore, J.S.W. acknowledges support from the UK EPSRC under Grant No. EP/S025065/1. O.S.H. and O.K. acknowledge support from the Oxford Centre for High Energy Density Science (OxCHEDS). This material is partially based on the work supported by the U.S. Department of Energy, Office of Science, Office of Fusion Energy Science under Award No. DE-SC0019268.

DATA AVAILABILITY

Raw data were generated at the European XFEL. Derived data supporting the findings of this study (10.22003/XFEL.EU-DATA-002191-00 and 10.22003/XFEL.EU-DATA-900099-00) are available from the corresponding author upon reasonable request.

REFERENCES

[1] A. H. Compton, "A quantum theory of the scattering of x-rays by light elements," Phys. Rev. **21**, 483–502 (1923).
[2] S. Huotari, K. Hämäläinen, S. Manninen, A. Issolah, and M. Marangolo, "Asymmetry of compton profiles," J. Phys. Chem. Solids **62**, 2205–2213 (2001).
[3] S. Huotari, J. A. Soininen, T. Pylkkänen, K. Hämäläinen, A. Issolah, A. Titov, J. McMinis, J. Kim, K. Esler, D. M. Ceperley, M. Holzmann, and V. Olevano, "Momentum distribution and renormalization factor in sodium and the electron gas," Phys. Rev. Lett. **105**, 086403 (2010).
[4] W. Schülke, H. Nagasawa, and S. Mourikis, "Dynamic structure factor of electrons in Li by inelastic synchrotron x-ray scattering," Phys. Rev. Lett. **52**, 2065–2068 (1984).
[5] W. Schülke, H. Nagasawa, S. Mourikis, and P. Lanzki, "Dynamic structure of electrons in Li metal: Inelastic synchrotron x-ray scattering results and interpretation beyond the random-phase approximation," Phys. Rev. B **33**, 6744–6757 (1986).
[6] C. Sternemann, A. Kaprolat, and W. Schülke, "Effect of thermal vibration and the solid-liquid phase transition on electron dynamics: An inelastic x-ray-scattering study on Al," Phys. Rev. B **57**, 622–626 (1998).
[7] E. Burkel, J. Peisl, and B. Dorner, "Observation of inelastic x-ray scattering from phonons," Europhys. Lett. **3**, 957–961 (1987).
[8] B. Dorner, E. Burkel, T. Illini, and J. Peisl, "First measurement of a phonon dispersion curve by inelastic x-ray scattering," Z. Phys. B: Condens. Matter **69**, 179–183 (1987).
[9] F. Sette, G. Ruocco, M. Krisch, U. Bergmann, C. Masciovecchio, V. Mazzacurati, G. Signorelli, and R. Verbeni, "Collective dynamics in water by high energy resolution inelastic x-ray scattering," Phys. Rev. Lett. **75**, 850–853 (1995).
[10] H. Sinn, F. Sette, U. Bergmann, C. Halcoussis, M. Krisch, R. Verbeni, and E. Burkel, "Coherent dynamic structure factor of liquid lithium by inelastic x-ray scattering," Phys. Rev. Lett. **78**, 1715–1718 (1997).
[11] E. Burkel, "Dynamics of new materials probed by inelastic x-ray scattering," Nucl. Instrum. Methods Phys. Res., Sect. B **199**, 143–150 (2003).
[12] A. Q. R. Baron, "Introduction to high-resolution inelastic x-ray scattering," arXiv:1504.01098v5.
[13] M. Krisch and F. Sette, "Inelastic x-ray scattering with very high resolution at the ESRF," Crystallogr. Rep. **62**, 1–12 (2017).
[14] J. D. Axe and G. Shirane, "Inelastic-neutron-scattering study of acoustic phonons in Nb_3Sn," Phys. Rev. B **8**, 1965–1977 (1973).
[15] F. Sette, M. H. Krisch, C. Masciovecchio, G. Ruocco, and G. Monaco, "Dynamics of glasses and glass-forming liquids studied by inelastic x-ray scattering," Science **280**, 1550–1555 (1998).
[16] I. Loa, L. F. Lundegaard, M. I. McMahon, S. R. Evans, A. Bossak, and M. Krisch, "Lattice dynamics of incommensurate composite Rb-IV and a realization of the monatomic linear chain model," Phys. Rev. Lett. **99**, 035501 (2007).
[17] C. Weis, C. Sternemann, V. Cerantola, C. J. Sahle, G. Spiekermann, M. Harder, Y. Forov, A. Kononov, R. Sakrowski, H. Yavaş, M. Tolan, and M. Wilke, "Pressure driven spin transition in siderite and magnesiosiderite single crystals," Sci. Rep. **7**, 16526 (2017).
[18] N. Murai, T. Fukuda, T. Kobayashi, M. Nakajima, H. Uchiyama, D. Ishikawa, S. Tsutsui, H. Nakamura, M. Machida, S. Miyasaka, S. Tajima, and A. Q. R. Baron, "Effect of magnetism on lattice dynamics in $SrFe_2As_2$ using high-resolution inelastic x-ray scattering," Phys. Rev. B **93**, 020301 (2016).

[19]S. H. Glenzer and R. Redmer, "X-ray Thomson scattering in high energy density plasmas," Rev. Mod. Phys. **81**, 1625–1663 (2009).
[20]H. J. Lee, P. Neumayer, J. Castor, T. Döppner, R. W. Falcone, C. Fortmann, B. A. Hammel, A. L. Kritcher, O. L. Landen, R. W. Lee, D. D. Meyerhofer, D. H. Munro, R. Redmer, S. P. Regan, S. Weber, and S. H. Glenzer, "X-ray Thomson-scattering measurements of density and temperature in shock-compressed beryllium," Phys. Rev. Lett. **102**, 115001 (2009).
[21]A. Höll, T. Bornath, L. Cao, T. Döppner, S. Düsterer, E. Förster, C. Fortmann, S. H. Glenzer, G. Gregori, T. Laarmann, K.-H. Meiwes-Broer, A. Przystawik, P. Radcliffe, R. Redmer, H. Reinholz, G. Röpke, R. Thiele, J. Tiggesbäumker, S. Toleikis, N. X. Truong, T. Tschentscher, I. Uschmann, and U. Zastrau, "Thomson scattering from near-solid density plasmas using soft x-ray free electron lasers," High Energy Density Phys. **3**, 120–130 (2007).
[22]P. Neumayer, C. Fortmann, T. Döppner, P. Davis, R. W. Falcone, A. L. Kritcher, O. L. Landen, H. J. Lee, R. W. Lee, C. Niemann, S. Le Pape, and S. H. Glenzer, "Plasmons in strongly coupled shock-compressed matter," Phys. Rev. Lett. **105**, 075003 (2010).
[23]L. B. Fletcher, E. Galtier, P. Heimann, H. J. Lee, B. Nagler, J. Welch, U. Zastrau, J. B. Hastings, and S. H. Glenzer, "Plasmon measurements with a seeded x-ray laser," J. Instrum. **8**, C11014 (2013).
[24]T. R. Preston, K. Appel, E. Brambrink, B. Chen, L. B. Fletcher, C. Fortmann-Grote, S. H. Glenzer, E. Granados, S. Göde, Z. Konôpková, H. J. Lee, H. Marquardt, E. E. McBride, B. Nagler, M. Nakatsutsumi, P. Sperling, B. B. L. Witte, and U. Zastrau, "Measurements of the momentum-dependence of plasmonic excitations in matter around 1 Mbar using an x-ray free electron laser," Appl. Phys. Lett. **114**, 014101 (2019).
[25]P. Sperling, E. J. Gamboa, H. J. Lee, H. K. Chung, E. Galtier, Y. Omarbakiyeva, H. Reinholz, G. Röpke, U. Zastrau, J. Hastings, L. B. Fletcher, and S. H. Glenzer, "Free-electron x-ray laser measurements of collisional-damped plasmons in isochorically heated warm dense matter," Phys. Rev. Lett. **115**, 115001 (2015).
[26]E. E. McBride, T. G. White, A. Descamps, L. B. Fletcher, K. Appel, F. P. Condamine, C. B. Curry, F. Dallari, S. Funk, E. Galtier, M. Gauthier, S. Goede, J. B. Kim, H. J. Lee, B. K. Ofori-Okai, M. Oliver, A. Rigby, C. Schoenwaelder, P. Sun, T. Tschentscher, B. B. L. Witte, U. Zastrau, G. Gregori, B. Nagler, J. Hastings, S. H. Glenzer, and G. Monaco, "Setup for meV-resolution inelastic x-ray scattering measurements and x-ray diffraction at the matter in extreme conditions endstation at the linac coherent light source," Rev. Sci. Instrum. **89**, 10F104 (2018).
[27]G. Gregori and D. O. Gericke, "Low frequency structural dynamics of warm dense matter," Phys. Plasmas **16**, 056306 (2009).
[28]H. R. Rüter and R. Redmer, "*Ab initio* simulations for the ion-ion structure factor of warm dense aluminum," Phys. Rev. Lett. **112**, 145007 (2014).
[29]B. B. L. Witte, L. B. Fletcher, E. Galtier, E. Gamboa, H. J. Lee, U. Zastrau, R. Redmer, S. H. Glenzer, and P. Sperling, "Warm dense matter demonstrating non-drude conductivity from observations of nonlinear plasmon damping," Phys. Rev. Lett. **118**, 225001 (2017).
[30]A. Descamps, B. K. Ofori-Okai, K. Appel, V. Cerantola, A. Comley, J. H. Eggert, L. B. Fletcher, D. O. Gericke, S. Göde, O. Humphries, O. Karnbach, A. Lazicki, R. Loetzsch, D. McGonegle, C. A. J. Palmer, C. Plueckthun, T. R. Preston, R. Redmer, D. G. Senesky, C. Strohm, I. Uschmann, T. G. White, L. Wollenweber, G. Monaco, J. S. Wark, J. B. Hastings, U. Zastrau, G. Gregori, S. H. Glenzer, and E. E. McBride, "An approach for the measurement of the bulk temperature of single crystal diamond using an x-ray free electron laser," Sci. Rep. **10**, 14564 (2020).
[31]P. Mabey, S. Richardson, T. G. White, L. B. Fletcher, S. H. Glenzer, N. J. Hartley, J. Vorberger, D. O. Gericke, and G. Gregori, "A strong diffusive ion mode in dense ionized matter predicted by Langevin dynamics," Nat. Commun. **8**, 14125 (2017).
[32]T. Tschentscher, C. Bressler, J. Grünert, A. Madsen, A. Mancuso, M. Meyer, A. Scherz, H. Sinn, and U. Zastrau, "Photon beam transport and scientific instruments at the European XFEL," Appl. Sci. **7**, 592 (2017).
[33]W. Decking, S. Abeghyan, P. Abramian, A. Abramsky, A. Aguirre, C. Albrecht, P. Alou, M. Altarelli, P. Altmann, K. Amyan, V. Anashin, E. Apostolov, K. Appel, D. Auguste, V. Ayvazyan, S. Baark, F. Babies, N. Baboi, P. Bak, V. Balandin, R. Baldinger, B. Baranasic, S. Barbanotti, O. Belikov, V. Belokurov, L. Belova, V. Belyakov, S. Berry, M. Bertucci, B. Beutner, A. Block, M. Blöcher, T. Böckmann, C. Bohm, M. Böhnert, V. Bondar, E. Bondarchuk, M. Bonezzi, P. Borowiec, C. Bösch, U. Bösenberg, A. Bosotti, R. Böspflug, M. Bousonville, E. Boyd, Y. Bozhko, A. Brand, J. Branlard, S. Briechle, F. Brinker, S. Brinker, R. Brinkmann, S. Brockhauser, O. Brovko, H. Brück, A. Brüdgam, L. Butkowski, T. Büttner, J. Calero, E. Castro-Carballo, G. Cattalanotto, J. Charrier, J. Chen, A. Cherepenko, V. Cheskidov, M. Chiodini, A. Chong, S. Choroba, M. Chorowski, D. Churanov, W. Cichalewski, M. Clausen, W. Clement, C. Cloué, J. A. Cobos, N. Coppola, S. Cunis, K. Czuba, M. Czwalinna, B. D'Almagne, J. Dammann, H. Danared, A. de Zubiaurre Wagner, A. Delfs, T. Delfs, F. Dietrich, T. Dietrich, M. Dohlus, M. Dommach, A. Donat, X. Dong, N. Doynikov, M. Dressel, M. Duda, P. Duda, H. Eckoldt, W. Ehsan, J. Eidam, F. Eints, C. Engling, U. Englisch, A. Ermakov, K. Escherich, J. Eschke, E. Saldin, M. Faesing, A. Fallou, M. Felber, M. Fenner, B. Fernandes, J. M. Fernández, S. Feuker, K. Filippakopoulos, K. Floettmann, V. Fogel, M. Fontaine, A. Francés, I. F. Martin, W. Freund, T. Freyermuth, M. Friedland, L. Fröhlich, M. Fusetti, J. Fydrych, A. Gallas, O. García, L. Garcia-Tabares, G. Geloni, N. Gerasimova, C. Gerth, P. Geßler, V. Gharibyan, M. Gloor, J. Głowinkowski, A. Goessel, Z. Gołkebiewski, N. Golubeva, W. Grabowski, W. Graeff, A. Grebentsov, M. Grecki, T. Grevsmuehl, M. Gross, U. Grosse-Wortmann, J. Grünert, S. Grunewald, P. Grzegory, G. Feng, H. Guler, G. Gusev, J. L. Gutierrez, L. Hagge, M. Hamberg, R. Hanneken, E. Harms, I. Hartl, A. Hauberg, S. Hauf, J. Hauschildt, J. Hauser, J. Havlicek, A. Hedqvist, N. Heidbrook, F. Hellberg, D. Henning, O. Hensler, T. Hermann, A. Hidvégi, M. Hierholzer, H. Hintz, F. Hoffmann, M. Hoffmann, M. Hoffmann, Y. Holler, M. Hüning, A. Ignatenko, M. Ilchen, A. Iluk, J. Iversen, J. Iversen, M. Izquierdo, L. Jachmann, N. Jardon, U. Jastrow, K. Jensch, J. Jensen, M. Jeżabek, M. Jidda, H. Jin, N. Johannson, R. Jonas, W. Kaabi, D. Kaefer, R. Kammering, H. Kapitza, S. Karabekyan, S. Karstensen, K. Kasprzak, V. Katalev, D. Keese, B. Keil, M. Kholopov, M. Killenberger, B. Kitaev, Y. Klimchenko, R. Klos, L. Knebel, A. Koch, M. Koepke, S. Köhler, W. Köhler, N. Kohlstrunk, Z. Konopkova, A. Konstantinov, W. Kook, W. Koprek, M. Körfer, O. Korth, A. Kosarev, K. Kosiński, D. Kostin, Y. Kot, A. Kotarba, T. Kozak, V. Kozak, R. Kramert, M. Krasilnikov, A. Krasnov, B. Krause, L. Kravchuk, O. Krebs, R. Kretschmer, J. Kreutzkamp, O. Kröplin, K. Krzysik, G. Kube, H. Kuehn, N. Kujala, V. Kulikov, V. Kuzminych, D. L. Civita, M. Lacroix, T. Lamb, A. Lancetov, M. Larsson, D. L. Pinvidic, S. Lederer, T. Lensch, D. Lenz, A. Leuschner, F. Levenhagen, Y. Li, J. Liebing, L. Lilje, T. Limberg, D. Lipka, B. List, J. Liu, S. Liu, B. Lorbeer, J. Lorkiewicz, H. H. Lu, F. Ludwig, K. Machau, W. Maciocha, C. Madec, C. Magueur, C. Maiano, I. Maksimova, K. Malcher, T. Maltezopoulos, E. Mamoshkina, B. Manschwetus, F. Marcellini, G. Marinkovic, T. Martinez, H. Martirosyan, W. Maschmann, M. Maslov, A. Matheisen, U. Mavric, J. Meißner, K. Meissner, M. Messerschmidt, N. Meyners, G. Michalski, P. Michelato, N. Mildner, M. Moe, F. Moglia, C. Mohr, S. Mohr, W. Möller, M. Mommerz, L. Monaco, C. Montiel, M. Moretti, I. Morozov, P. Morozov, D. Mross, J. Mueller, C. Müller, J. Müller, K. Müller, J. Munilla, A. Münnich, V. Muratov, O. Napoly, B. Näser, N. Nefedov, R. Neumann, R. Neumann, N. Ngada, D. Noelle, F. Obier, I. Okunev, J. A. Oliver, M. Omet, A. Oppelt, A. Ottmar, M. Oublaid, C. Pagani, R. Paparella, V. Paramonov, C. Peitzmann, J. Penning, A. Perus, F. Peters, B. Petersen, A. Petrov, I. Petrov, S. Pfeiffer, J. Pflüger, S. Philipp, Y. Pienaud, P. Pierini, S. Pivovarov, M. Planas, E. Pławski, M. Pohl, J. Polinski, V. Popov, S. Prat, J. Prenting, G. Priebe, H. Pryschelski, K. Przygoda, E. Pyata, B. Racky, A. Rathjen, W. Ratuschni, S. Regnaud-Campderros, K. Rehlich, D. Reschke, C. Robson, J. Roever, M. Roggli, J. Rothenburg, E. Rusiński, R. Rybaniec, H. Sahling, M. Salmani, L. Samoylova, D. Sanzone, F. Saretzki, O. Sawlanski, J. Schaffran, H. Schlarb, M. Schlösser, V. Schlott, C. Schmidt, F. Schmidt-Foehre, M. Schmitz, M. Schmökel, T. Schnautz, E. Schneidmiller, M. Scholz, B. Schöneburg, J. Schultze, C. Schulz, A. Schwarz, J. Sekutowicz, D. Sellmann, E. Semenov, S. Serkez, D. Sertore, N. Shehzad, P. Shemarykin, L. Shi, M. Sienkiewicz, D. Sikora, M. Sikorski, A. Silenzi, C. Simon, W. Singer, X. Singer, H. Sinn, K. Sinram, N. Skvorodnev, P. Smirnow, T. Sommer, A. Sorokin, M. Stadler, M. Steckel, B. Steffen, N. Steinhau-Kühl, F. Stephan, M. Stodulski, M. Stolper, A. Sulimov, R. Susen, J. Świerblewski, C. Sydlo, E. Syresin, V. Sytchev, J. Szuba, N. Tesch, J. Thie, A. Thiebault, K. Tiedtke, D. Tischhauser, J. Tolkiehn, S. Tomin, F. Tonisch, F. Toral, I. Torbin, A. Trapp, D. Treyer, G. Trowitzsch, T. Trublet, T. Tschentscher, F. Ullrich, M. Vannoni, P. Varela, G. Varghese, G. Vashchenko, M. Vasic, C. Vazquez-Velez, A. Verguet, S. Vilcins-Czvitkovits, R. Villanueva, B. Visentin, M. Viti, E. Vogel, E. Volobuev, R. Wagner, N. Walker, T. Wamsat, H. Weddig, G. Weichert, H. Weise, R. Wenndorf, M. Werner,

R. Wichmann, C. Wiebers, M. Wiencek, T. Wilksen, I. Will, L. Winkelmann, M. Winkowski, K. Wittenburg, A. Witzig, P. Wlk, T. Wohlenberg, M. Wojciechowski, F. Wolff-Fabris, G. Wrochna, K. Wrona, M. Yakopov, B. Yang, F. Yang, M. Yurkov, I. Zagorodnov, P. Zalden, A. Zavadtsev, D. Zavadtsev, A. Zhirnov, A. Zhukov, V. Ziemann, A. Zolotov, N. Zolotukhina, F. Zummack, and D. Zybin, "A MHz-repetition-rate hard x-ray free-electron laser driven by a superconducting linear accelerator," Nat. Photonics **14**, 391 (2020).

[34]S. Abeghyan, M. Bagha-Shanjani, G. Chen, U. Englisch, S. Karabekyan, Y. Li, F. Preisskorn, F. Wolff-Fabris, M. Wuenschel, M. Yakopov, and J. Pflueger, "First operation of the SASE1 undulator system of the European x-ray free-electron laser," J. Synchrotron Radiat. **26**, 302–310 (2019).

[35]H. Sinn, M. Dommach, B. Dickert, M. Di Felice, X. Dong, J. Eidam, D. Finze, I. Freijo-Martin, N. Gerasimova, N. Kohlstrunk, D. La Civita, F. Meyn, V. Music, M. Neumann, M. Petrich, B. Rio, L. Samoylova, S. Schmidtchen, M. Störmer, A. Trapp, M. Vannoni, R. Villanueva, and F. Yang, "The SASE1 x-ray beam transport system," J. Synchrotron Radiat. **26**, 692–699 (2019).

[36]T. Maltezopoulos, F. Dietrich, W. Freund, U. F. Jastrow, A. Koch, J. Laksman, J. Liu, M. Planas, A. A. Sorokin, K. Tiedtke, and J. Grünert, "Operation of x-ray gas monitors at the European XFEL," J. Synchrotron Radiat. **26**, 1045–1051 (2019).

[37]X. Dong, D. Shu, and H. Sinn, "Design of a cryo-cooled artificial channel-cut crystal monochromator for the European XFEL," AIP Conf. Proc. **1741**, 040027 (2016).

[38]J. Grünert, M. P. Carbonell, F. Dietrich, T. Falk, W. Freund, A. Koch, N. Kujala, J. Laksman, J. Liu, T. Maltezopoulos, K. Tiedtke, U. F. Jastrow, A. Sorokin, E. Syresin, A. Grebentsov, and O. Brovko, "X-ray photon diagnostics at the European XFEL," J. Synchrotron Radiat. **26**, 1422–1431 (2019).

[39]P. Mason, S. Banerjee, J. Smith, T. Butcher, J. Phillips, H. Höppner, D. Möller, K. Ertel, M. De Vido, I. Hollingham, A. Norton, S. Tomlinson, T. Zata, J. S. Merchan, C. Hooker, M. Tyldesley, T. Toncian, C. Hernandez-Gomez, C. Edwards, and J. Collier, "Development of a 100 J, 10 Hz laser for compression experiments at the high energy density instrument at the European XFEL," High Power Laser Sci. Eng. **6**, e65 (2018).

[40]See www.hibef.eu for information on the HIBEF user consortium and its contributions to the HED instrument at the European XFEL.

[41]B. Lengeler, C. G. Schroer, B. Benner, T. F. Günzler, M. Kuhlmann, J. Tümmler, A. S. Simionovici, M. Drakopoulos, A. Snigirev, and I. Snigireva, "Parabolic refractive x-ray lenses: A breakthrough in x-ray optics," Nucl. Instrum. Methods Phys. Res., Sect. A **467-468**, 944–950 (2001).

[42]C. Masciovecchio, U. Bergmann, M. Krisch, G. Ruocco, F. Sette, and R. Verbeni, "A perfect crystal x-ray analyser with meV energy resolution," Nucl. Instrum. Methods Phys. Res., Sect. B **111**, 181–186 (1996).

[43]C. Masciovecchio, U. Bergmann, M. Krisch, G. Ruocco, F. Sette, and R. Verbeni, "A perfect crystal x-ray analyser with 1.5 meV energy resolution," Nucl. Instrum. Methods Phys. Res., Sect. B **117**, 339–340 (1996).

[44]R. Verbeni, M. Kocsis, S. Huotari, M. Krisch, G. Monaco, F. Sette, and G. Vanko, "Advances in crystal analyzers for inelastic x-ray scattering," J. Phys. Chem. Solids **66**, 2299–2305 (2005).

[45]H. H. Johann, "Die erzeugung lichtstarker röntgenspektren mit hilfe von konkavkristallen," Z. Phys. **69**, 185–206 (1931).

[46]J. W. M. DuMond and H. A. Kirkpatrick, "A direct spectrum of the structure and shift of the Compton line with helium gas as the scatterer," Phys. Rev. **52**, 419–436 (1937).

[47]S. Huotari, G. Vankó, F. Albergamo, C. Ponchut, H. Graafsma, C. Henriquet, R. Verbeni, and G. Monaco, "Improving the performance of high-resolution x-ray spectrometers with position-sensitive pixel detectors," J. Synchrotron Radiat. **12**, 467–472 (2005).

[48]S. Huotari, F. Albergamo, G. Vankó, R. Verbeni, and G. Monaco, "Resonant inelastic hard x-ray scattering with diced analyzer crystals and position-sensitive detectors," Rev. Sci. Instrum. **77**, 053102 (2006).

[49]G. Blaj, P. Caragiulo, G. Carini, S. Carron, A. Dragone, D. Freytag, G. Haller, P. Hart, J. Hasi, R. Herbst, S. Herrmann, C. Kenney, B. Markovic, K. Nishimura, S. Osier, J. Pines, B. Reese, J. Segal, A. Tomada, and M. Weaver, "X-ray detectors at the linac coherent light source," J. Synchrotron Radiat. **22**, 577–583 (2015).

[50]D. Windisch and P. Becker, "Silicon lattice parameters as an absolute scale of length for high precision measurements of fundamental constants," Phys. Status Solidi A **118**, 379–388 (1990).

[51]G. Geloni, V. Kocharyan, and E. Saldin, "A novel self-seeding scheme for hard x-ray FELs," J. Mod. Opt. **58**, 1391–1403 (2011).